3. Neutron Emission Profile Measurement

3.1 Introduction

Neutron diagnostics is one of the most important diagnostics for control of burning plasmas for future fusion devices like ITER [1]. Because neutrons are uncharged, they are able to escape immediately from the plasma and, hence, can be detected. Above all, a measurement of neutron emission profile is of great importance for the knowledge of the profile of fusion power and the source of alpha particles.

Neutron profile emission measurement is main and important diagnostics in ITER [2, 3]. Line integrated neutron emissivity along collimated chords of a fan shaped array, which view inwardly through a midplane port and spans as much as possible of the plasma cross-section, is measured in neutron emission profile. Summation of the chordal signals, together with knowledge of the plasma major radius, gives the global neutron source strength, hence total fusion power. Two fan shaped collimated arrays, the horizontal array and the vertical array will be designed in ITER. Combined horizontal data with vertical data, allow tomographic reconstruction of the spatial distribution of neutron emssivity, $n_D n_T \langle \sigma v \rangle$, which determines the alpha particle source profile and fusion power density, and constrains inferred values of effective ion temperature.

Therefore establishment of a measurement method of neutron profile is highly desirable. In large tokamak devices like JET and TFTR, multi-channel neutron diagnostics system is installed in order to measure neutron profiles [4, 5].

In JT-60U, neutron emission profile measurement has been started by installing 6 channel neutron emission profile monitor. Firstly, As neutron detector to start with, NE213 organic liquid scintillators [6] were used, which are widely used for neutron measurements because of their good time resolution and well-known efficiency. Although it was expected that the signals of outermost channel were small, these signals were, however, about 40 % as much as that of innermost channel in the experiment using NE213 scintillator. The main reason is considered to be gamma-rays background.

Because organic scintillators such as NE213 organic liquid scintillator are sensitive not only to neutrons but also to gamma-rays. Therefore investigation of behavior on neutrons only is impossible. In order to eliminate gamma-ray effects, another module for discrimination between neutrons and gamma-rays is necessary [7, 8].

Then, we applied Stilbene neutron detectors. Recently the Stilbene neutron detector has been developed by TRINITI laboratory in Russia. This detector combines a Stilbene organic crystal scintillator with a neutron Gamma pulse shape discrimination circuit. This has enabled us to detect only neutrons except for gamma-rays in the experiment. The Stilbene neutron detectors have been installed 6 channel neutron emission profile monitor for the neutron emission profile measurement.
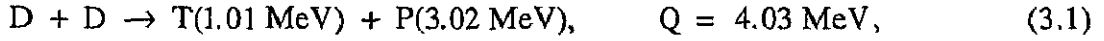
In this chapter, firstly, the necessary theoretical background for fusion neutron is provided in section 3.2. Then, diagnostics system of neutron emission profile measurement is presented in section 3.3. The instrument of neutron emission profile measurement is described in Sec. 3.3.1. In Sec. 3.3.2 results of measurement using NE213 scintillator are described. We explain the Stilbene neutron detector and also its calibration in Sec. 3.3.3. The calculation for shielding and scattering effects by a general Monte Carlo code is presented in Sec. 3.3.4. Finally we report the first result of neutron emission profile measurement using Stilbene neutron detector in Sec. 3.4, and summary of this chapter is presented in Sec. 3.5.

3.2. Theoretical background of the fusion neutron emission

The emitted neutron rate from a plasma is a weighted average of the velocity distribution with cross section and relative velocity. Present-day fusion devices for magnetically confined plasma experiments are usually operating by deuterium fuel for simulation of reactor plasmas. Neutron diagnostics basically installed. In this section fusion reactions, fusion cross sections and fusion reactivities are presented.

3.2.1. Fusion reactions and their cross section

The main fusion reactions in a tokamak plasma relevant for neutron diagnostics are the following:

$$D + D \rightarrow T(1.01\,\text{MeV}) + P(3.02\,\text{MeV}), \qquad Q = 4.03\,\text{MeV}, \qquad (3.1)$$

$$D + D \rightarrow {}^{3}\text{He}(0.82\,\text{MeV}) + n(2.45\,\text{MeV}), \qquad Q = 3.27\,\text{MeV}, \qquad (3.2)$$

$$D + T \rightarrow {}^{4}\text{He}(3.56\,\text{MeV}) + n(14.03\,\text{MeV}), \qquad Q = 17.59\,\text{MeV}, \qquad (3.3)$$

$$T + T \rightarrow {}^{4}\text{He}(3.78\,\text{MeV}) + 2n(7.56\,\text{MeV}), \qquad Q = 11.34\,\text{MeV}. \qquad (3.4)$$

In the above given equations, the reaction Q-values and, in addition, the particle energies for zero-energy reactants are given where appropriate. The two branches of the D-D reaction occur with nearly equal probability.

The interpretation of neutron source strength measurements in present fusion devices or the prediction of the fusion power gain of future experiments requires accurate knowledge of the relevant fusion cross sections. In particular, since measured fusion rates are of increasing importance for plasma diagnostics on large fusion experiments, the uncertainties in the cross sections are required to be of the order or less than the errors in neutron source strength measurements.

Since about 1945, many measurements of the fusion cross sections have been carried out. However, reliable experimental data are not available for energies below about 10 keV and even for the limited experimental energy range available the measurements are not always in agreement.

Therefore, it is necessary to extrapolate downwards using theoretical formulas. Furthermore, analytical representations of the fusion cross sections are desirable for calculations of fusion reaction rates. As shown in Fig.3.1, the cross section varies over more than 10 orders of magnitude over the energy range 1000 keV. Due to the strong dependence on the particle energy it has been found most convenient to represent the cross section as

$$\sigma(E) = S(E)\,(1/E)\exp\left(-B_G / \sqrt{E}\right), \qquad (3.5)$$

where E denotes the energy in the centre-of-mass frame and $B_G = \pi \alpha Z_A Z_B \sqrt{2\mu_{red}C^2}$ is

the Gamov constant for reacting particles with atomic numbers Z_A and Z_B. Here, $\mu_{red} = m_A m_B / (m_A + m_B)$ is the reduced mass and α is the fine structure constant. The exponential term in Eq.(3.5) describes simply the tunnelling probability and was first given by Gamov [9]. The factor 1/E results from the quantum mechanical description of the fusion probability, and S is the astrophysical S-function [10]. Thus, the cross section is factorized into terms describing the well-known and strongly energy-dependent quantum mechanical processes and a term which refers solely to nuclear processes of the fusion reaction. For energies below about 90 keV in the case of D-D reactions and about 30 keV for D-T reactions, the S-function can be written as

$$S(E) \approx \beta \exp(-\gamma E). \tag{3.6}$$

The parameter β, γ and B_G are given in Table 3.1.

Two approximate analytical representations of the fusion cross sections for a wide energy range have been widely used until recently. The first has been derived by Duane [11], which is also given in the NRL (Naval Research Laboratory) formulary [12], and the other has been derived by Peres [13]. Recently, improved formulae for the cross sections have been given by Bosch and Hale [14] which provide a higher degree of accuracy than the previous analytical representations. The paper by Bosch and Hale also contains a useful survey over the relevant literature concerning the measured cross section data and different evaluations. The improvement in the cross section representation could be achieved by fitting the S-function data obtained from R-matrix analysis [15] with a Padé polynomial as

$$S(E) = \frac{a_1 + E(a_2 + E(a_3 + E(a_4 + a_5 E)))}{b_1 + E(b_2 + E(b_3 + E(b_4 + b_5 E)))}. \tag{3.7}$$

Reaction	β (barn kev)	γ (keV^{-1})	B_G (keV$^{1/2}$)
D-D	52.6	-5.8×10^{-3}	31.397
D-T	9821	-2.9×10^{-2}	34.827

Table 3.1 *Low-energy parameterization of the cross section in the centre-of-mass system.*
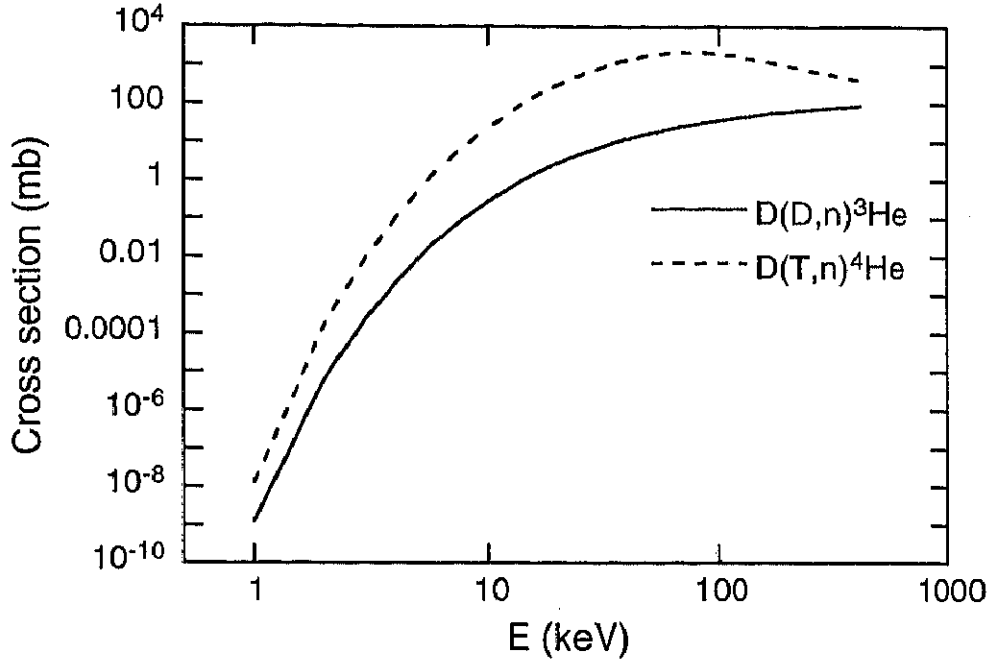
Figure 3.1 *Fusion cross section for the fusion reaction* $D(D,n)^3He$ *reaction and* $D(T,n)^4He$ *as a function in the center-of-mass-frame (from Ref.[14]).*

New parameterizations were given for the reactions $D(D,n)^3He$, $D(T,n)^4He$, $D(D,p)t$ and $^3He(D,p)^4He$. The fit results for the neutron producing D-D and D-T reactions are shown in Table 3.2.

3.2.2. Fusion reactivities

The local fusion reaction rate R for a plasma containing ion species of types A and B is given by

$$R = \frac{n_A n_B}{1 + \delta_{AB}} \langle \sigma v \rangle_{AB} \qquad (3.8)$$

where n_A and n_B are the particle densities and δ_{AB} is the Kronecker symbol. The reactivity $\langle \sigma v \rangle_{AB}$ is in general given by the six-dimensional integral

$$\langle \sigma v \rangle_{AB} = \iint f_A(\mathbf{v}_A) f_B(\mathbf{v}_B) \sigma(|\mathbf{v}_A - \mathbf{v}_B|) |\mathbf{v}_A - \mathbf{v}_B| d\mathbf{v}_A d\mathbf{v}_B, \qquad (3.9)$$

where f_A, f_B are the normalized velocity distributions of the reacting particles, σ is the

Coefficient	Reaction	
	D(D,n)³He	D(T,n)⁴He
a1	5.3701×10^4	6.927×10^4
a2	3.3027×10^2	7.454×10^8
a3	-1.2706×10^{-1}	2.050×10^6
a4	2.9327×10^{-5}	5.2002×10^4
a5	-2.5151×10^{-9}	0.0
b1	1	1
b2	0.0	6.38×10^1
b3	0.0	-9.95×10^{-1}
b4	0.0	6.981×10^{-5}
b5	0.0	1.728×10^{-4}
E range (keV)	0.5-4900	0.5-550
$(\Delta S)_{max}$ (%)	2.5	1.9

Table 3.2 *Parameters for the cross section fit in the centre-of-mass system in units of mb for the D(D,n)3He and the D(T,n)4He fusion reactions, respectively (from Ref.[14]).*

cross section and $|v_A - v_B|$ is the velocity of impact. For this integration considerable analytic simplification can be achieved by choosing a spherical coordinate system for velocity space and assuming azimuthal symmetry [16]. With the assumption of azimuthal symmetry, the distribution functions are of the form $f_K(v, \mu)$, where $v = |v|$ and $\mu = v_\parallel / v = \cos\theta$ is the cosine of the pitch angle, and can be expanded in Legendre polynomials P_n as

$$f_K(v,\mu) = \sum_{n=0}^{\infty} k_n(v) P_n(\mu).$$

One obtains the following simplified expression:

$$\langle \sigma v \rangle_{AB} = 4\pi^2 \sum_{n=0}^{\infty} \frac{2}{2n+1} \int_0^\infty a_n(v_A) \int_0^\infty b_n(v_B) \int_{-1}^{1} P_n(\mu_{AB}) \sigma(u) u d\mu_{AB} dv_A dv_B. \tag{3.10}$$

Here, a_n and b_n are the nth-order coefficient functions from the expansion of the ion distributions in Legendre polynomials (thus reducing the number of integration to be performed), $\mu_{AB} = \cos(\theta_A - \theta_B)$ and $u^2 = v_A^2 + v_B^2 - 2v_A v_B \mu_{AB}$.

Eq.(3.10) is valid for arbitrary two-dimensional distribution functions. However, it is of interest to consider two special cases for which expression (3.10) can be further simplified. Firstly, for the interaction of a fast monoenergetic particle population with velocity v_0 with a Maxwellian plasma with temperature T one obtains [17, 18]

$$\langle \sigma v \rangle_{AB} = \frac{1}{v_0 v_A \sqrt{\pi}} \int_0^\infty \sigma(v)v^2 \left[\exp\left(-\frac{m_A(v-v_0)^2}{2T} \right) - \exp\left(-\frac{m_A(v+v_0)^2}{2T} \right) \right] dv. \quad (3.11)$$

Secondly, for a thermal plasma with two interacting Maxwellian ion species of the same temperature, expression (3.10) reduces to [18]

$$\langle \sigma v \rangle_{AB} = \frac{2}{\sqrt{\pi}} \left(\frac{\mu_{red}}{2T} \right)^{3/2} \int_0^\infty v^3 \sigma(v) \exp\left(-\frac{\mu_{red} v^2}{2T} \right) dv. \quad (3.12)$$

On using the approximate low-temperature formula (3.6) for the S-function in expression (3.5) of the cross section, the Maxwellian fusion reactivity simplifies to [12]

$$\langle \sigma v \rangle_{AB} = k_{AB} T^{-2/3} \exp(-\lambda_{AB} T^{-1/3}) \approx k_{AB}^* T^K. \quad (3.13)$$

It should be noted that the overall agreement of reactivities calculated using this expression with correct results using the rather accurate cross section fit given by Bosch and Hale is barely sufficient for reasonable estimates. The following more complicated, but rather accurate parameterized form for the thermal reactivities has been given by Bosch and Hale [14]:

$$\langle \sigma v \rangle = c_1 \theta (\xi / \mu_{red} c^2 T^3)^{1/2} \exp(-3\xi) \, ,$$

$$\theta = T \left(1 - \frac{R(c_2 + T(c_4 + Tc_6))}{1 + T(c_3 + T(c_5 + Tc_7))} \right)^{-1} , \quad (3.14)$$

$$\xi = (B_B^2 / 4\theta)^{1/3} \, .$$

Here, the reactivity is in $cm^3 s^{-1}$ and the parameters resulting from this fit are shown in Table 3.3.for the temperature range 0.2-100 keV. Other published results can be found in Refs.[19, 20].

However, by minor empirical modification of the simplified expression (3.13), a much better approximate expression can be obtained and is given by

$$\langle \sigma v \rangle_{AB} = k_{AB} \sqrt{T} \exp(-3\eta_{AB} T^{-1/3}). \quad (3.15)$$

Coefficient	Reaction	
	$D(D,n)^3He$	$D(T,n)^4He$
$\mu_{red}c^2$(keV)	937 814	1 124 656
c_1	5.43360×10^{12}	1.17302×10^{-9}
c_2	5.85778×10^{-3}	1.51361×10^{-2}
c_3	7.68222×10^{-3}	7.51886×10^{-2}
c_4	0.0	4.60643×10^{-3}
c_5	-2.96400×10^{-6}	1.35000×10^{-2}
c_6	0.0	-1.06750×10^{-4}
c_7	0.0	1.36600×10^{-5}
T range (keV)	0.2-100	0.2-100

Table 3.3 *Parameters for the thermal reactivity fit for the $D(D,n)^3He$ and the $D(T,n)^4He$ fusion reactions, respectively (from Ref. [19])*

Here, the temperature is in keV and the reactivity is again in cm^3s^{-1}. Furthermore,

$$k_{DD} = 2.33 \times 10^{-14} \ cm^3s^{-1}, \quad \eta_{DD} = 6.27, \quad k_{DT} = 6.68 \times 10^{-12} cm^3 \ s^{-1} \quad \text{and} \quad \eta_{DT} = 6.66,$$

respectively.

Comparing the expression (3.15) with the fit results from Bosch and Hale, Eq.(3.14), the agreement is in the temperature range from 3.5 to 37 keV better than 5% for the DD reaction. In the temperature range from 5 to 28 keV the agreement is better than 2 %. Only below 1 keV, down to 0.1 keV, the error is increasing from about 18% to about 43 % for the DD reaction. For the D-T reaction this approximate expression is accurate to less than 20 % in the temperature range from 0.1 to 22 keV and in the temperature range from 8 to 19.5 keV the agreement is better than 11 %.

3.3 Diagnostics system of neutron emission profile measurement of JT-60U

3.3.1 Neutron emission profile monitor

The instrument of neutron emission profile measurement is comprised of six channel collimator array ($2.6m \times 1.3m \times 1.6m$) viewing a poloidal cross section through

the plasma and is located about 5 m away from the plasma center as shown in Fig. 3.2.

The sight line of each collimator channel is constrained by the space available in the JT-60U torus hall. As illustrated in Fig. 3.2, one of the sight lines of 6 collimator channels passes though the center (R = 3.3 m, z = 0 m) of the vacuum vessel, the others are oriented to measure along the off-axis chords. The structure of neutron collimator array is shown in Fig. 3.3. The collimator array utilizes Polyethylene assemblies to shield against neutron out of the sight line of each channel. Lead reduces a gamma-ray generated by neutrons incident to Polyethylene and a backscattered gamma-ray from the external structures of JT-60U device. The housing of the neutron detector is surrounded by soft magnetic iron to remove the influence of magnetic field. The size of each collimator tube is 30 mm$^\Phi$ $\times$ 800 mm ^{L} . Where Φ and L are the diameter of the
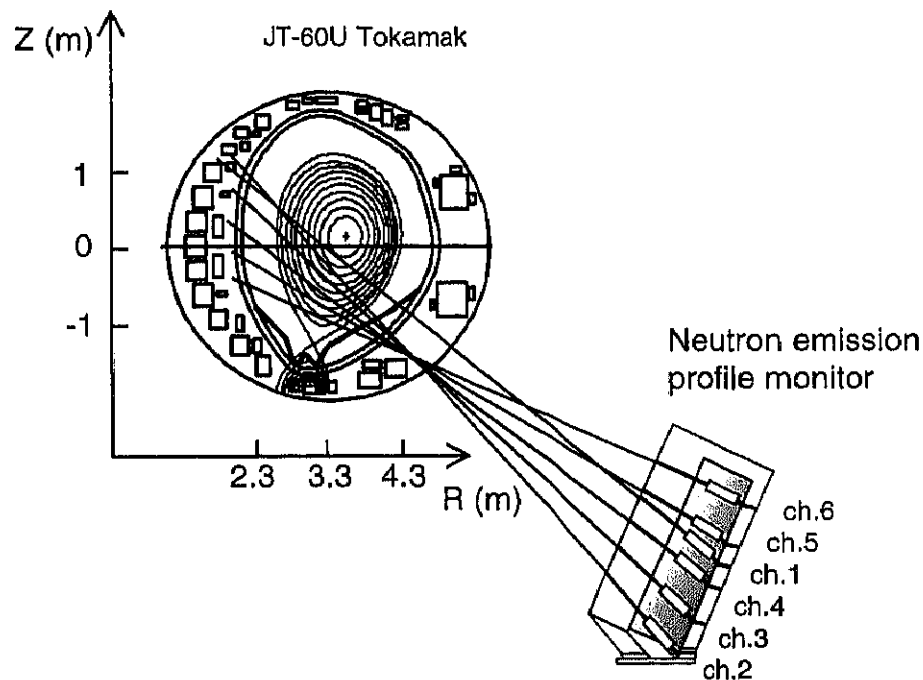
Figure 3.2 *Illustration of the JT-60U neutron emission profile monitor and its collimation geometry. The line-of-sight chord the viewing poloidal cross section of the plasma.*

(a)

PolyetheIne
lead
detector box

30mm$^\Phi$×800
mm ^{L}
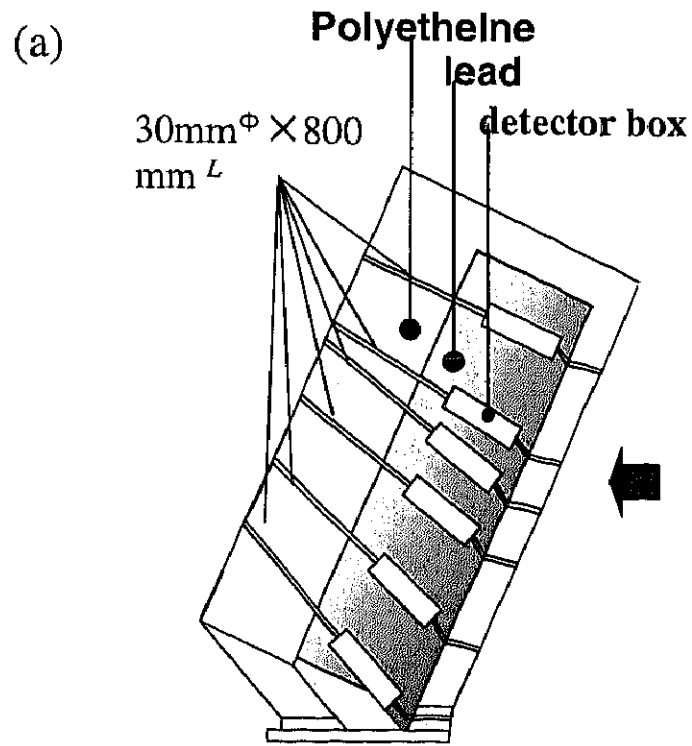
(b)
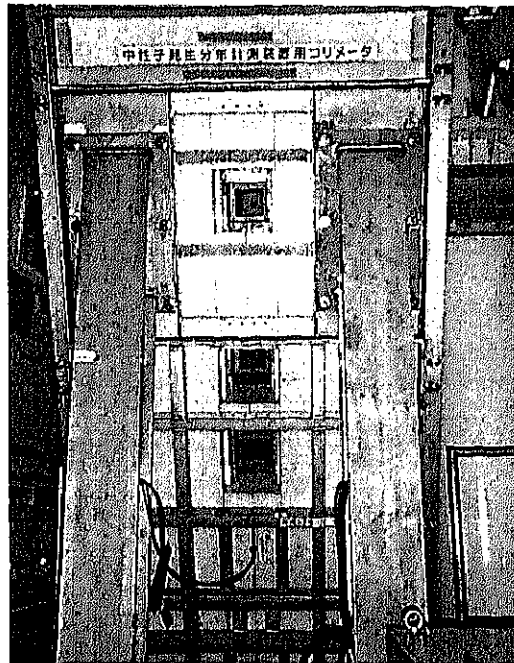
Figure 3.3 *(a) Structure of six-channel collimator array   (b) the picture of rear of neutron collimator*

aperture and the length of collimator, respectively. The viewing extent of each collimator channel at R =3.3 m is about 200 mm. We can change the aperture size of collimator channel to 20 mm$^\Phi$, 15 mm$^\Phi$, 12 mm$^\Phi$ and 10 mm$^\Phi$ depending on the experimental condition. Furthermore, we can install Pb plug of 10 cm in length to attenuate gamma-ray flux for high performance experiments such as total neutron emission rate is over 10^{16} n/s. Because the count rate limit of Stilbene neutron detector depends on the sum of neutron flux and gamma-ray flux. It is calculated that neutron flux reduction by Pb plug is only 5.3 for neutron energy over 1MeV.

3.3.2 Neutron detector

3.3.2.1 The principle of measurement

To start with neutron emission profile measurements, NE213 organic liquid scintillator had been used. In this section, the principle of measurement of an organic scintillator such as NE213 scintillator is briefly explained.

The production of light in organic scintillators is the result of molecular transitions. Consider the energy-level diagram of Fig.3.4, which shows how the potential energy of a molecule changes with interatmic distance. The ground state of the molecule ia at point A0, which coincides with the minimum of the potential energy. Ionizing radiation passing through the scintillator may give energy to the molecule and raise it to an excite state, i.e., the transition $A_0 \rightarrow A_1$ may occur. The position A_1 is not the point of minimum energy. The molecule will release energy through lattice vibration (that energy is eventually dissipated as heat) and move to point B_1. The point B_1 is still an excited state and, in some cases, the molecule will undergo the transition $B_1 \rightarrow B_0$ accompanied by the emission of the photon with energy equal to $E_{B1}-E_{B0}$. This transition, if allowed, take place at time of the order of 10^{-8} s. It should be noted that the energy of the emitted photon ($E_{B1}-E_{B0}$) is less than the energy that caused the excitation ($E_{A1}-E_{A0}$). This difference is very important because otherwise the emission spectrum of the scintillator would completely coincide with its absorption spectrum and no scintillations would be
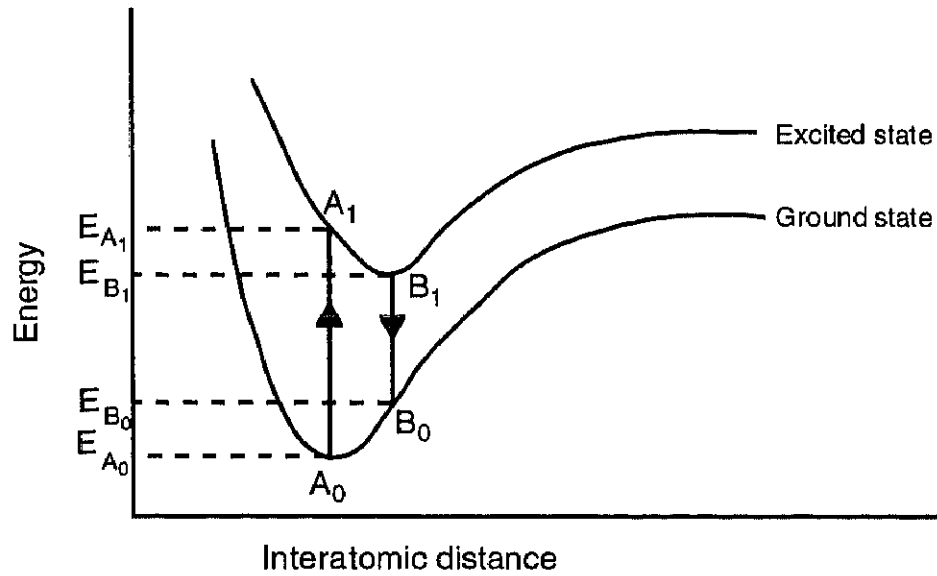
Figure 3.4 *The proton energy distribution after a (n, p) collision that is isotropic in the center of mass system of the two particles*

produced.

The most important additional conversion process useful for fast neutrons is elastic neutron scattering. In this interaction an incident neutron transfers a portion of its kinetic energy to scattering nucleus, giving rise to a recoil nucleus.

Since neutrons and protons have approximately the same mass, a neutron may, in one collision, transfer all its kinetic energy to the proton. However, there is a possibility that the struck proton may have any energy between zero and full neutron energy. As a result, the relationship between a neutron energy spectrum and a pulse-height distribution of the struck protons is not simple. It is the objective of this section to derive a general expression for this relationship. The section that follow show its application for specific detectors.

Consider the case of a neutron with kinetic energy E_n colliding with a proton at rest. To calculate the proton kinetic energy after the collision, one must apply the equations of conservation of energy and linear momentum using $M_n = M_p$. The result for E_p, the proton kinetic energy as a function of the recoil angle θ, is

$$E_p = E_n \cos^2 \theta$$

In a neutron –proton collision, the maximum value of angle θ is $90°$, and the minimum $0°$; therefore, the limits of the proton energy are $0 < E_p < E_n$. For neutron energies up to about 14MeV, the (n-P) collision is isotropic in the center-of-mass system; as a consequence, there is an equal probability for the proton to have any energy between zero and E_n. That is, if p(E)dE is the probability that the proton energy in between E and E+dE, after the collision, then

$$p(E)dE = \frac{dE}{E_n}.$$

What is important for observer is not p(E) but the proton pulse-height distribution produced by the detector.

3.3.2.2 Measurement by using NE213 scintillator

The NE213 scintillator, which is one of organic scintillators of the NE series, is most commonly used and studied in detail. This consists of xylene ($C_6H_4(CH_3)_2$), activators, the organic compound POPOP ($C_{24}H_{16}N_2O_2$), as a wavelength shifter), and naphthalene, which is added to improve light emission. The density of NE213 is about 870 kg/m^3, and its composition is taken to be $CH_{1.21}$.

We installed NE213 scintillator (25.4mm$^\phi$× 25.4mm ^{l}) to neutron emission profile monitor as shown in Fig 3.3 and applied this to JT-60U experiments. Firstly, we confirmed the linearity of the NE213 detector of the profile monitor. Figure 3.5 shows that the count rate of the NE213 detector is linearly proportional to the neutron flux from the ^{235}U fission chamber (FC). We can see that the count rate of the NE213 detector was deviated from the linearity at a neutron flux of $1.0×10^{16}$ neutrons/s of the FC. We confirmed that the neutron emission profile measurements are reliable up to neutron flux of $1.0×10^{16}$ neutrons/s of the FC.

Example of neutron emission profile measured by using NE213 scintillator during Neutral Beam (NB) injection was shown. Figure 3.6 (a) and (b) show the time trace of

14

12

10

8

6

4

2

0

NE213 count-rate (10^5 s^{-1})

0   5   10   15

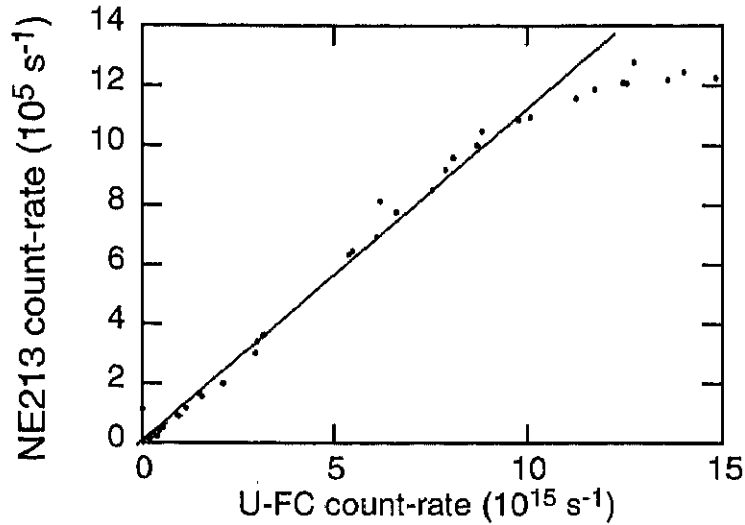U-FC count-rate (10^{15} s^{-1})

Figure 3.5 *Linearity of NE213 scintillator for total neutron emission rate by U-FC*

the input power of NB and neutron emission rate of each channel measured by neutron emission profile monitor, respectively. The plasma configuration and sight lines of neutron emission profile monitor at t = 8.6s are shown in Fig. 3.7. The sight line of innermost channel passes through r/a ~0.15 and the outermost channel passes through r/a ~ 0.85, where r/a is the normalized minor radius. As the input power of NB increases, neutron emission rate of each channel increases. The signal of the innermost channel is the largest. However, the signal of the outermost channel is about 40 % as much as that of innermost channel as shown in Fig.3.8. It is considered that the signals of outermost channel were small, since the density and temperature of bulk plasma are relatively low and there is not beam deposition in the region of r/a > 0.85. This can be caused by gamma-ray background. Because organic scintillators such as NE213 scintillator are sensitive not only to neutrons but also to gamma-rays as described in previous section.

Therefore investigation of the pure neutron behavior is impossible. In order to eliminate gamma-ray effects, the discrimination between neutrons and gamma-rays is necessary.
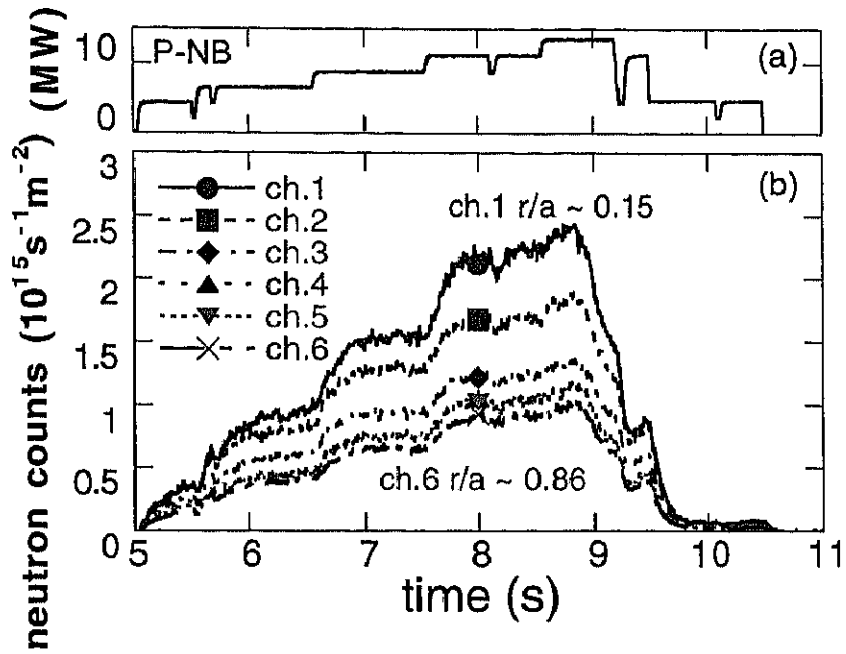
Figure 3.6 *Wave forms of E37818 discharge. (a) Input power of neutral beam(b) Neutron signal for each channel.*
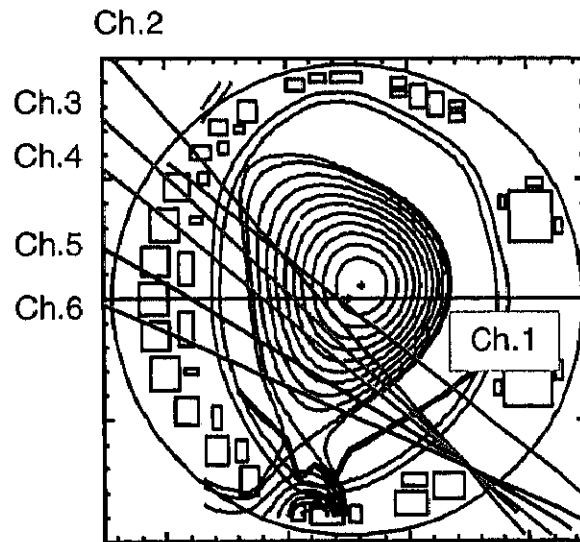

Figure 3.7 *The plasma configuration at t = 8.6 s, E37818 and the sight line of neutron emission profile measurement. The innermost channel passes through r/a~0.15, and outermost channel passes through r/a~0.85.*

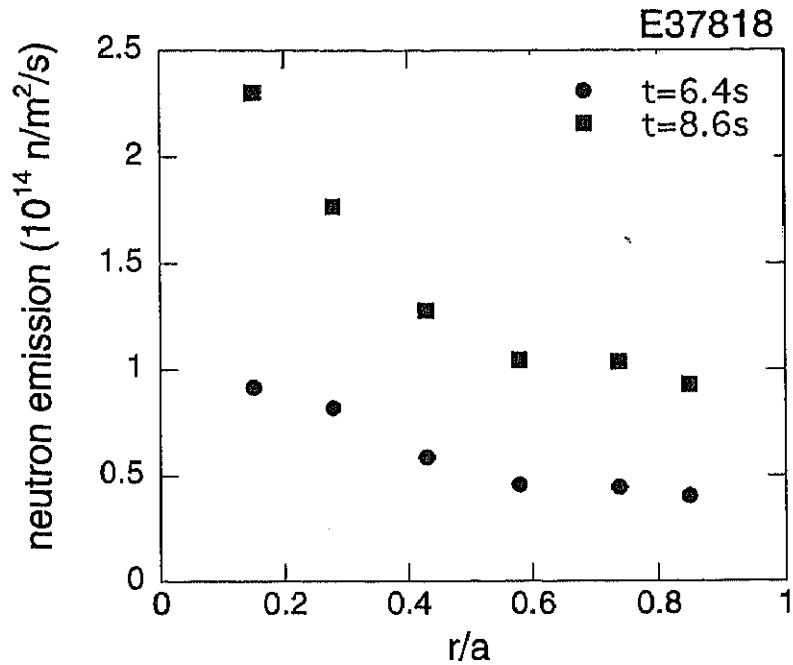Figure 3.8 *Profiles of line-integrated neutron emission by NE213 scintillator. The signal of outermost channel is about 40 % as much as that of innermost channel.*

Then, we applied Stilbene neutron detector in order to detect only neutrons in our experiments. Recently the Stilbene neutron detector has been developed by TRINITI laboratory in Russia. In next section the explanation about Stilbene neutron detector is presented.

3.3.2.3 Stilbene neutron detector

3.3.2.3.1 Structure of Stilbene Neutron Detector

The Stilbene neutron detector combines a Stilbene organic crystal scintillator with a neutron-gamma pulse shape discrimination circuit. The structure of Stilbene neutron detector is shown in Fig. 3.9 (a). The rear panel of the Stilbene neutron detector is illustrated in Fig.3.9 (b). This detector has two outputs. One is LINEAR output, which provides unipolar pulses linearly proportional in peak amplitude to energy of neutrons or gamma-rays. The other is CONTROL output, which provides an Emitter Coupled Logic

(ECL) signal when a neutron ($E_n > E_{thr}$) is detected, where E_n is the detected neutron energy and E_{thr} is the threshold energy decided by the electronic circuit. Power to Photomultiplier and electronic is supplied from the input of HV and POWER, respectively.

Stilbene crystal scintillation part ·

Stilbene crystal in the Stilbene neutron detector is used as the scintillator material. The size of Stilbene crystal is 30 mm$^\phi \times$ 30 mm^L. Stilbene has a density of 1.16×10^3 kg/m^3 and short decay time of scintillation light of 4~8 ns. Characteristic of Stilbene crystal, together with Anthracene and NE213, is shown in table 3.4. The principle of measurement of the Stilbene is essentially the same as NE213 scintillator. The Stilbene has an excellent pulse shape discrimination property. It allows discrimination between scintillation by charged particles induced by neutrons and electrons induced by gamma-rays. It is notice that Stilbene crystals are sensitive to thermal and mechanical shock.

Photomultiplier and Electronic circuit

As photomultiplier (PMT), ELT 9266B type manufactured by Electron Tube Ltd. is used, which is superior to low dark current and low background noise. Figure 3.10 shows the voltage divider of ELT 9266B. The light output of the detected scintillation pulse in the Stilbene crystal is converted to an electronic signal and amplified by the PMT. The amplified signals are passed to the electronic circuit.

The block diagram inside the electronic circuit is illustrated in Fig.3.11. PMT, DY and ANOD mean photomultiplier, a dynode and an anode, respectively. The CONTROL output and the LINEAR output are generated through the following process. The signals from the anode (ANOD) and the last dynode (DY10) of the photomultiplier are used for Pulse Shape Discriminator (PSD). A method of PSD integrates the charge from the early part of the pulse and compares it to the total charge. The detailed method of PSD is given
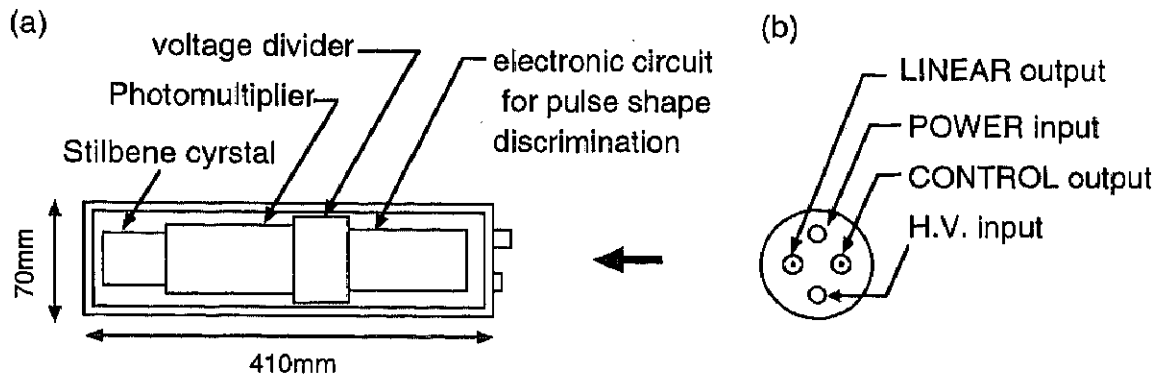
Figure 3.9 *(a)Structure of a Stilbene neutron detector. A Stilbene neutron detector consists of a Stilbene scintillator and an electronic circuit for discrimination between neutron and gamma-ray, (b) rare panel of the Stilbene neutron detector. The Stilbene neutron detector has two output : one is LINEAR output and the other is CONTOL output.*

	Type	Density [g/cm^3]	Light output [% of Anth.]	Max emission Wavelengh, [mm]	Main decay Time [ns]	Ratio No of H atoms / No of C atoms
Anthracene	C	1.25	100	447	33.0	0.715
Stilbene	C	1.16	80	410	4.05	0.858
NE213	L	0.87	50	425	3.16	1.213

Table 3.4 *Properties of organic scintillators. C and L mean Crystal and Liquid in the column of Type, respectively*

in Appendix. Gamma-rays are discriminated here. While the signal from the middle dynode (DY6) is also to set a fixed threshold level to eliminate all pulses with an amplitude below a given size to remove inevitable noise pulses and background events. Then by taking the coincidence of these two signals and passing them to Single Pulse Generator, only when the neutron energy is over the threshold level, an ECL logic signal is emitted. This is the CONTROL output. The signal from DY6 also is used for an output as a linear signal, too. This is the LINEAR Output.
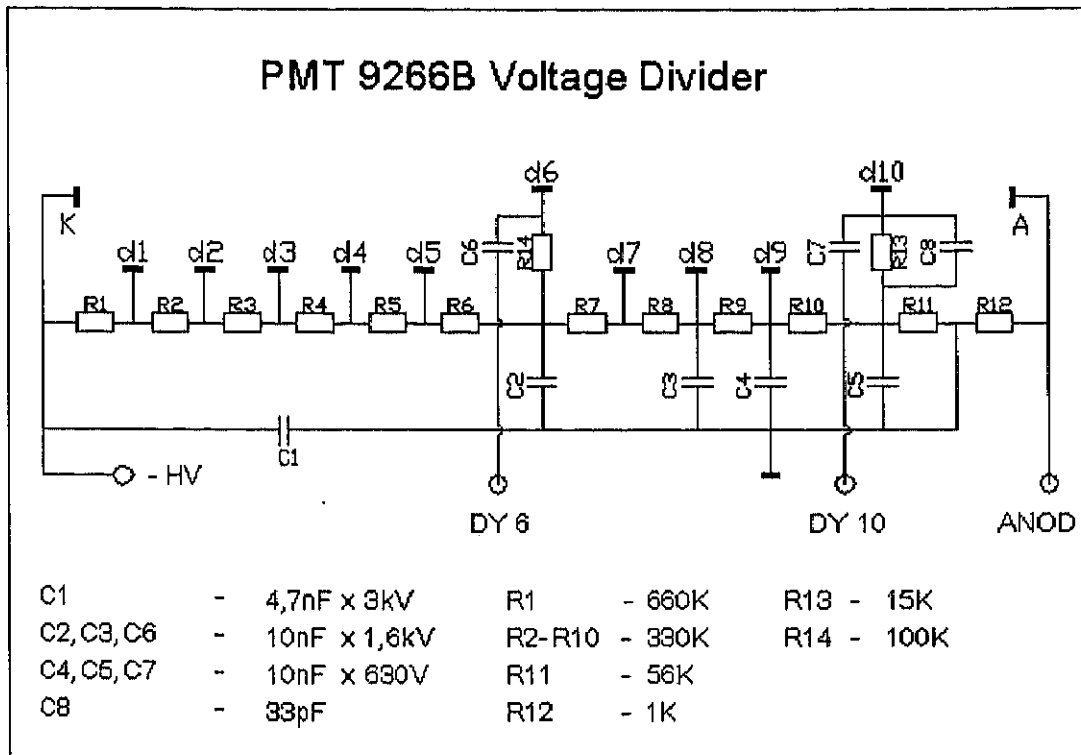
PMT 9266B Voltage Divider

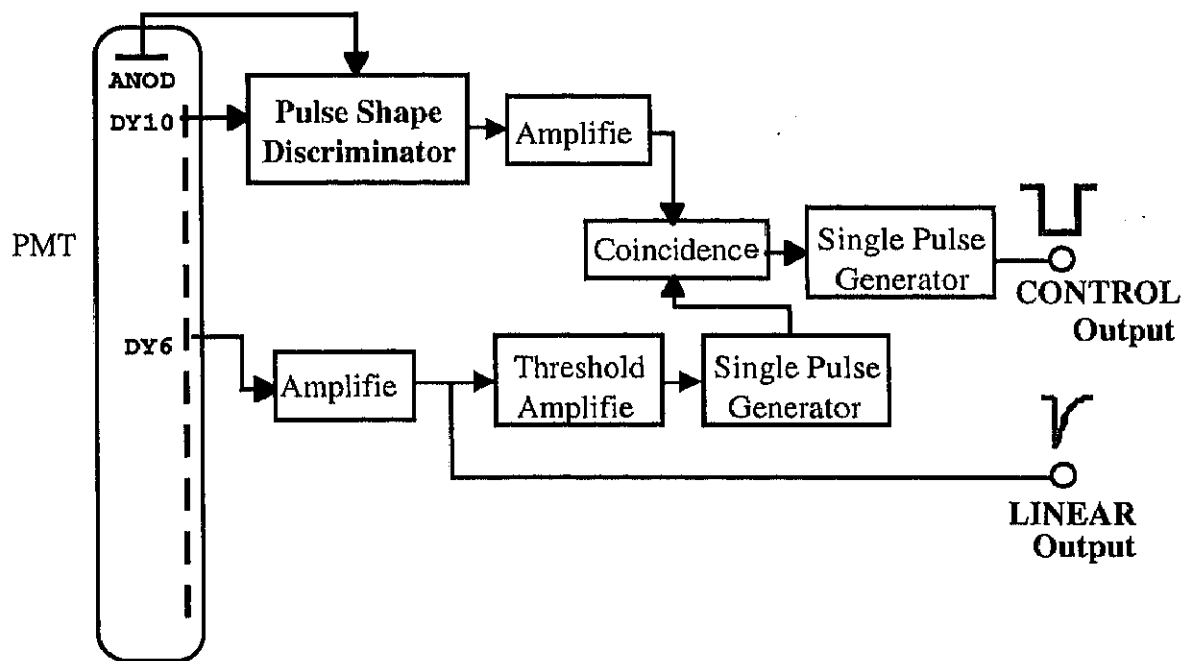|				
C1	–	4,7nF x 3kV	R1	– 660K	R13 – 15K
C2,C3,C6	–	10nF x 1,6kV	R2-R10	– 330K	R14 – 100K
C4,C5,C7	–	10nF x 630V	R11	– 56K	
C8	–	33pF	R12	– 1K	

Figure 3.10 *Illustration of PMT 8266B Voltage Divider*

Figure 3.11 *Block diagram inside the electronic circuit of the Stilbene neutron detector*

The size of Stilbene neutron detector (70 mm$^\Phi$ $\times$ 410 mm^L) is almost the same as a standard organic scintillator with a similar scintilltaion size. Generally, an additional module is necessary to discriminate neutrons from gamma-rays. However, a Stilbene crystal scintillator combined with an electronic circuit for pulse shape discrimination eliminates the need of additional module, and is very compact. This detector is very useful for multi-channel measurements.

3.3.2.3.2 Calibration of Stilbne neutron detector using neutron and gamma-ray source

Neutron and gamma-ray sources were used to check the operation of Stilbene neutron detector to verify its property of neutron-gamma pulse shape discrimination.

The LINEAR output, which provides unipolar pulses with peak amplitudes linearly proportional to the energy of neutrons or gamma-rays as described in the previous section, is used to check the pulse height spectrum of neutrons and gamma-rays. If the ECL logic signal from the CONTROL output is utilized as a gate signal when we check the pulse height spectrum, then we can obtain the pulse height spectrum of neutrons only. A schematic diagram of experimental setup of this calibration is shown in Fig. 3.12. In this case, the threshold level of the CONTROL output is set at 300 ch. We compared the pulse height spectrum with the gate (GATED signal) and without the gate (LINEAR signal).

In the first calibration, a gamma-ray source ^{137}Cs was used. ^{137}Cs emits gamma-ray at 662keV but emits no neutron. So the CONTROL output is expected to provide no signal. The pulse height spectrum for the GATED signal of ^{137}Cs is compared with the LINEAR signal in Fig. 3.13 (a) together with the number of integrated counts for the GATED output. The pulse height spectrum for the LINEAR signal has a Compton edge corresponding to the energy of a gamma-ray from ^{137}Cs. A pulse for the GATED signal was not detected as expected. We verified that Stilbene neutron detector can sufficiently suppress gamma-ray signals.
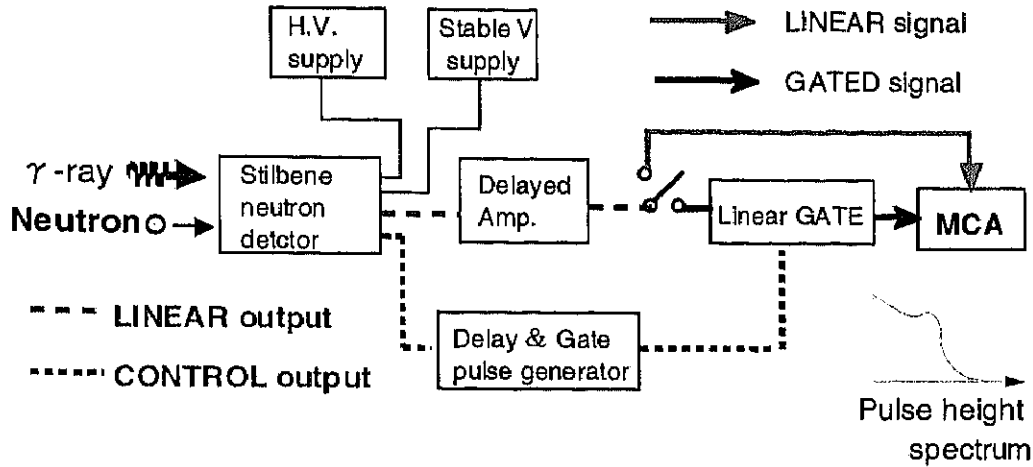
47

Figure 3.12 *Schematic of experimental setup of Stilbene neutron detector calibration*

In the second calibration, we used ^{252}Cf neutron source, which is widely used for calibration of neuron detectors. The energy spectrum of neutrons radiated from ^{252}Cf is approximately expressed by

$$\frac{dN}{dE} \propto E^{1/2} e^{-E/1.42},$$

where E is neutron energy in MeV [21]. Simultaneously much gamma-ray is also radiated from ^{252}Cf. The pulse height spectrum of ^{252}Cf is shown in Fig. 3.13 (b). In the case of GATED signal, pulse heights below the threshold level were eliminated.

In the third calibration, neutron and gamma-ray sources were set at the same time. The pulse height spectrum and the number of integrated counts for GATED signal (^{252}Cf $+^{137}$Cs) were in a good agreement with those using only ^{252}Cf as shown in Fig. 3.13 (c). These results show that the CONTROL output provides an output signal when a neutron radiated from ^{252}Cf with its energy over the threshold is detected. We can verify that the CONTROL output of the Stilbene neutron detector suppresses gamma-ray sufficiently and provides the signal only when neutron is detected in these calibration.
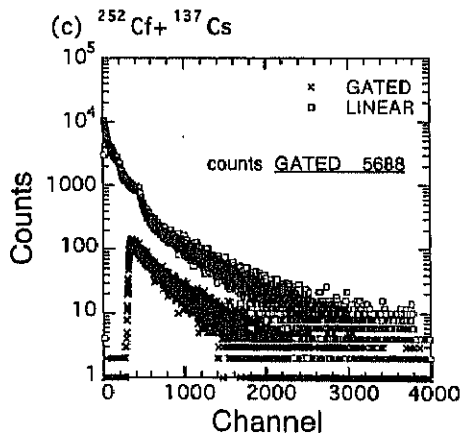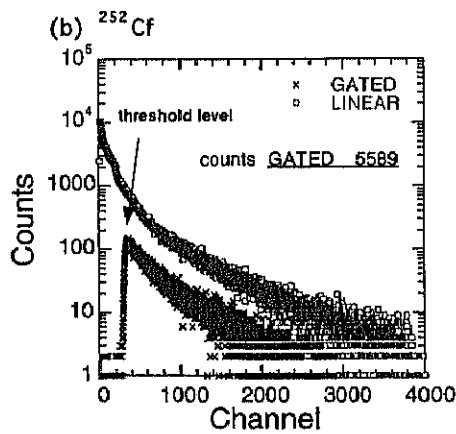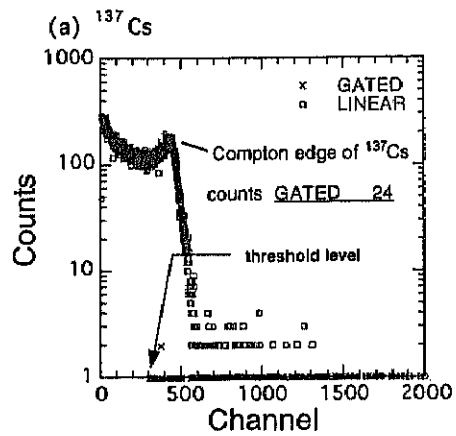
Figure 3.13 *Pulse height spectrum of Stilbene neutron detector in the calibration using neutron and gamma-ray sources. The GATED signal (crosses) is compared with the LINEAR signal (squares). (a) Gamma-ray source ^{137}Cs, (b) Neutron source ^{252}Cf, (c) Mixture $^{252}Cf+$ ^{137}Cs. Number of counts of the Gated signal for a measurement time of 3 minute is given in each figure. In the case of (a), the GATED signal is hardly counted. While, there is an agreement within a statistics error between (b) and (c).*

We confirmed the relation between the gamma-ray energy and the pulse height of Stilbene neutron detector using three kinds of gamma-ray source: [137]Cs (the radiated energy is 662 keV), [22]Na (511, 1274 keV) and [60]Co (1173, 1333 keV). By using the relation between neutron energy and gamma-ray energy for the pulse height of Stilbene scintillator [22], we could set up the threshold energy E_{thr} at 1 MeV.

3.3.2.3.3 Performance test in DD neutron field in Fusion Neutronics Source

A performance test of Stilbene neutron detector was performed on Fusion Neutronics Source (FNS) in JAERI Tokai [23]. The FNS facility is an intense D-T neutron source for fusion neutronics study. D-T neutron, up to $\sim 10^{13}$ n/s, is produced by striking accelerated 400keV deuteron into the tritium target (DT operation). By changing the target from tritium to deuterium gas, DD neutron can be also produced (DD operation).

The DD operation was used to simulate deuterium plasma in a JT-60U experiment. The result of this test is shown in Fig.3.14. The pulse height spectrum of LINEAR signal suggested single energy neutron and simultaneously several kinds of gamma-ray were produced. While the pulse height spectrum of GATED signal was a box type, showing that only mono-energy neutrons produced by DD reactions are detected as mentioned in Sec. 3.3.2.2.1. In range of $10^2 \sim 10^5$ counts per second (cps), the operation of the Stilbene neutron detector was demonstrated under existence of background gamma-rays.

The electronic circuit as well as the Stilbene crystal of the Stilbene neutron detector is in the sight line in the present neutron measurement system as shown in Fig. 3.3. However, the neutron flux which is incident to the sight line is usually $10^4 \sim 10^5$ cps in our DD experiment. Therefore the Stilbene neutron detector is applicable to JT-60U experiments.
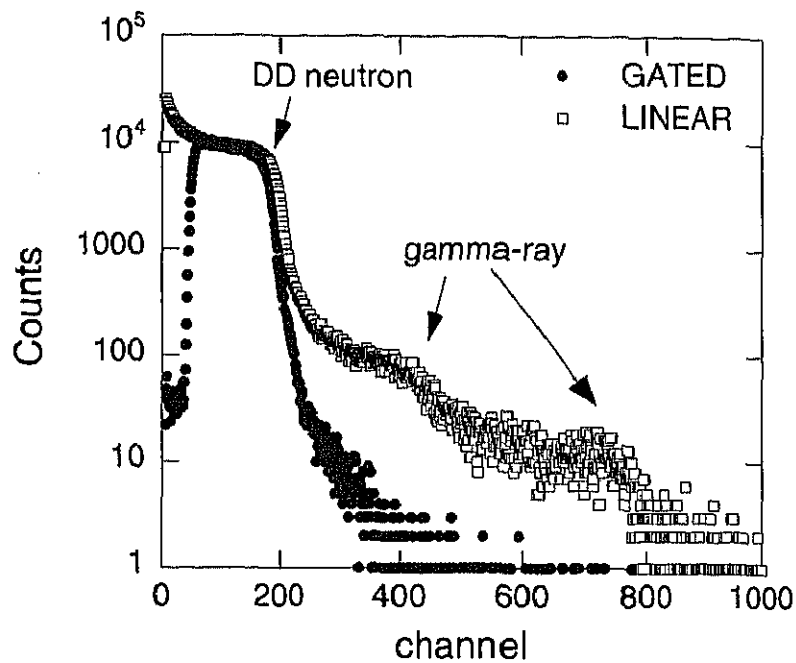
Figure 3.14 *Pulse height spectrum of the Stilbene neutron detector in DD operation in FNS. Closed circles are GATE signals and open squares are LINEAR signals.*

3.3.2.3.4 Neutron detection efficiency

The absolute neutron detection efficiency for one of the Stilbene neutron detectors was determined on DD operation in FNS. The absolute neutron efficiency was measured to be 5.6 $\times$ 10^{-2} per incident neutron for the threshold energy of 1 MeV.

Also relative efficiencies of 6 Stilbene neutron detectors were checked using the ^{252}Cf neutron source in the same condition. It was shown that the neutron detection efficiency is the same within ±5 %. We use the actual measured neutron detection efficiency for each detector in the experiment in JT-60U.

A relative calibration was performed for the same detector after the first experimental campaign for two months using the ^{252}Cf neutron source. For all the detectors the change in sensitivity is within 4 % before and after the first experimental campaign.

51

3.3.3 Calculation of neutron attenuation and scattering

Since the fusion neutrons are attenuated when they pass through the structural material of the vacuum vessel, correction of attenuation is required for absolute neutron flux measurement. It is also necessary to consider the effect of neutron scattering in the collimator walls. A general Monte Carlo Code for Neutron and Photon Transport (MCNP) [24] is used to estimate these correction factors.

MCNP is a general-purpose and continuous-energy Monte Carlo code that can be used for neutron, photon, or coupled neutron/photon transport, including the capability to calculate eigenvalues for critical system. It solves neutral particle transport problems and may be used in any of three modes: neutron transport only, photon transport only, or combined neutron/photon transport, where the photons are produced by neutron interactions. The code treats an arbitrary three-dimensional configuration of material in geometric cell bounded by first- and second-degree surface and some special fourth-degree surface (elliptical tori). Pointwise cross-section data are used. For neutrons, all reactions given in a particular cross-section evaluation are account for. For photon, the code takes account of incoherent and coherent scattering, the possibility of fluorescent emission after photoelectric absorption, and absorption in pair production with local emission of annihilation radiation. The neutron energy regime is from 10-11 MeV to 20 MeV, and the photon energy regime is from 1 keV to 100 MeV.

To carry out the calculation of MCNP code, a geometric configuration of the system is necessary. In this model, the system consists of only the vacuum vessel and the neutron collimator. Since the sight line of this measurement is between the toroidal field coil, we do not include the toroidal field coil in our model. We assume that the vacuum vessel is an elliptic cylinder whose length is 4 m and the port window in the sight line is added to the vessel as illustrated in Fig. 3.15 (a). We assume that the neutron collimator is a rectangular, but the thickness of Polyethylene and lead, and also the length of collimator are set to be the same of the real collimator illustrated in Fig. 3.3.
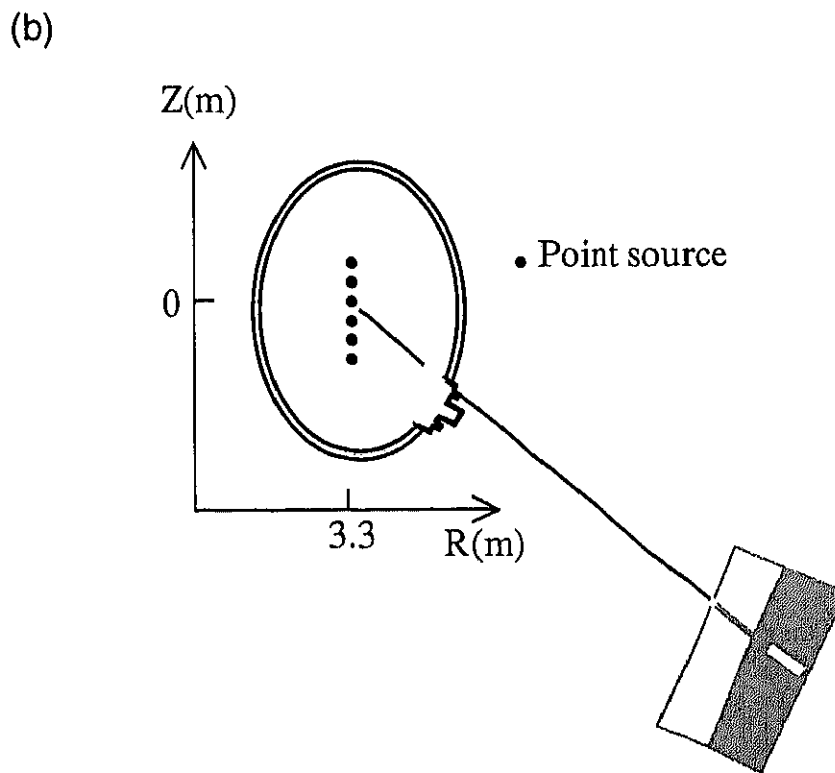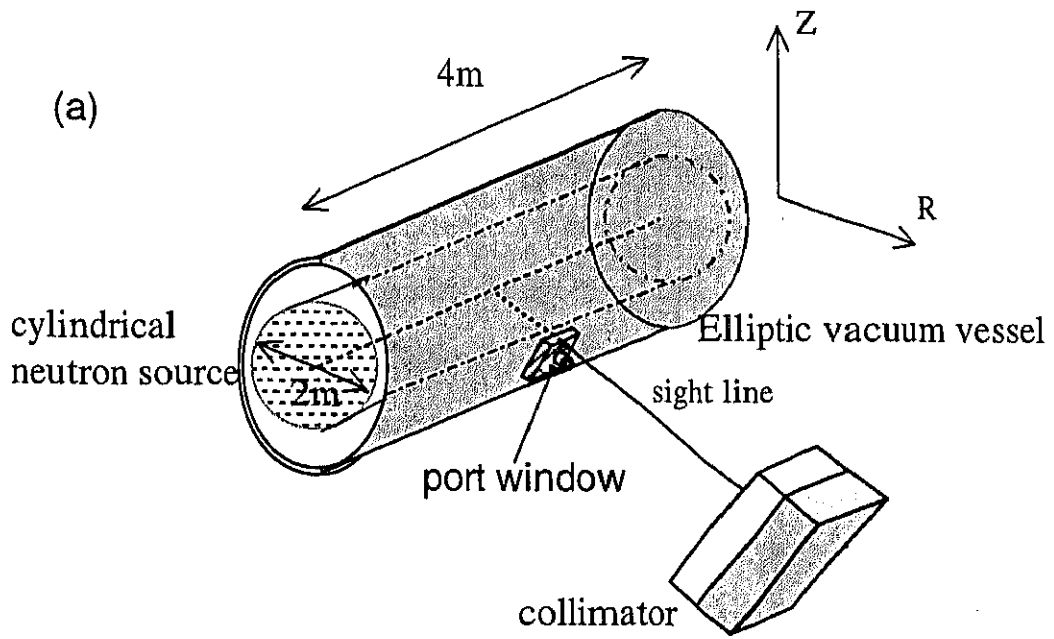
Figure 3.15 *(a) Geometric configuration of the calculation of MCNP code. (b) Cross section on the sight line of geometric configuration. The neutron point source is scanned vertically at R=3.3m.*

To estimate the effects of attenuation by the vacuum vessel and scattering by collimator wall separately, we performed the calculation with three different models. The First one considers attenuation and scattering by the vacuum vessel and the neutron collimator. This corresponds to a normal experimental condition (Normal model). In the second model, the vacuum vessel is removed from Normal model to investigate the effect of the vacuum vessel (No V.V. model). In the last model, the geometric configuration is the same as the No V.V. model. However, if neutrons hit the collimator wall, we assume that the neutrons disappear without scattering or penetration. It means that the last model is the same as an ideal optical model (Optical model).

In the calculation, we compare the neutron detection efficiencies according to the above three models by scanning the 2.45 MeV point neutron source. Figure 3.15 (b) shows the cross section (R-Z plane) of the geometric configuration illustrated in Fig. 3.15 (a) together with the point neutron source. The point source is scanned vertically at R = 3.3 m.

Figure 3.16 shows the energy spectrum of the detected neutron in the case of Normal model. We can see that some of 2.45 MeV neutrons from the source are scattered at the collimator wall. Figure 3.17 shows the difference of the efficiencies according to the above three models. The X-axis is the position of the point neutron source as shown in Fig. 3.15 (b). The difference between the Normal model (triangles) and the No V.V. model (closed squares) is small. This suggests that the effect of attenuation and scattering by the vacuum vessel is small. On the other hand, neutron detection efficiency in the case of the Optical model (open squares) is smaller than that in the case of the Normal model. Since neutron hitting the collimator wall disappears in the case of the Optical model, it means that the difference is caused by scattering of neutrons in the collimator assembly. The number of neutrons whose energy larger than 1 MeV is evaluated to be 69.5 % to the total number of neutrons in Fig. 3.16. As shown in the section 3.2, the Stilbene neutron
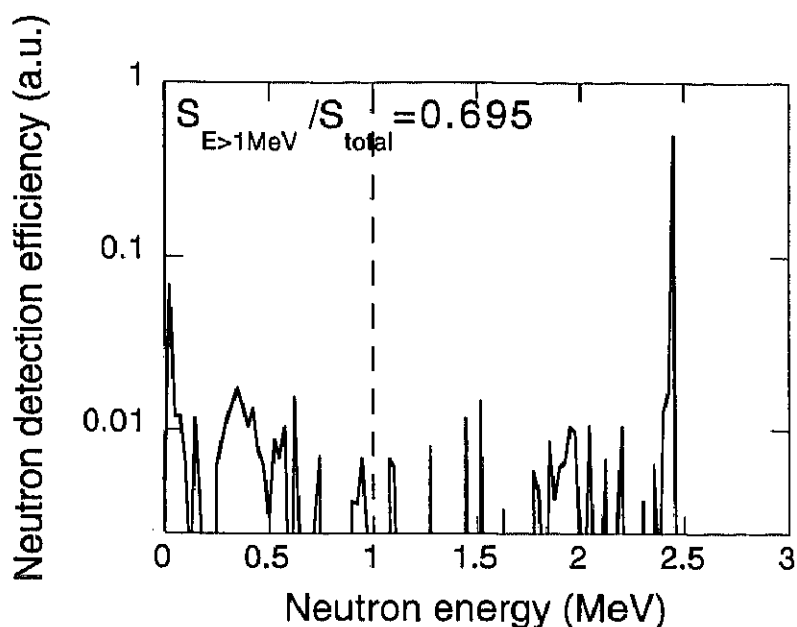
Figure 3.16 *Energy spectrum of neutrons in the case of Normal model*

detector is adjusted to measure the neutron with energy larger than 1 MeV, then this number of 69.5 % is important to calibrate the absolute measurement. The circles in Fig. 3.17 show the neutron detection efficiency in the Normal model with neutron energy over 1 MeV ($E \geqq 1$ MeV). Figure 3.17 shows that the difference between the Normal model ($E \geqq 1$ MeV) and the Optical model becomes small in the range of $E \geqq 1$ MeV. Assuming a homogeneous cylindrical neutron source, the correction factor for the Normal model ($E \geqq 1$ MeV) compared with the Optical model is 1.08.

3.3.4 Data acquisition system

The data acquisition system of the neutron emission profile measurement is illustrated in Fig.3.18. In the present system we use only ECL logic signal from CONTROL output of the Stilbene neutron detector. Because this output is corresponding to neutron events. This output is fed to ECL-TTL converter. Converted TTL signal is further converted to an optical signal by TTL E/O (JAERI model) in order to feed the signal from Torus hall to the data acquisition room (Shield room). The optical signal is then converted to electric signal by TTL O/E (JAERI model) again and is counted by the
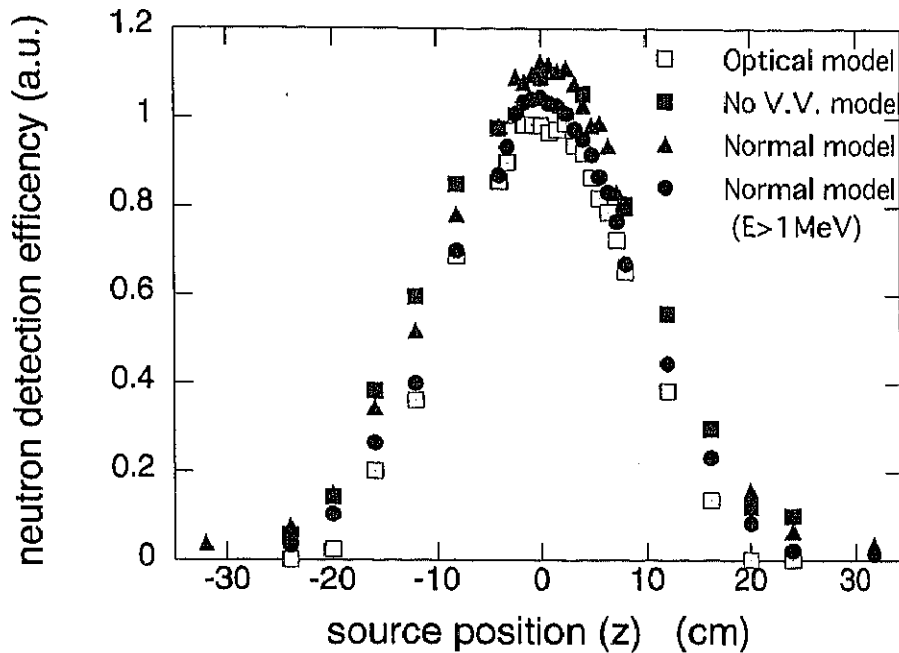
Figure 3.17 *Neutron detection efficiency of three models: the Normal model (triangles), the No V.V. model (closed squares), the Optical model (open square), and Normal model with neutron energy over 1 MeV (closed circles) calculated by the MCNP code*

scaler (LeCroy model 8590). And the information is stored every 10ms by the memory module (LeCroy model 8201) in a normal operation. These data management of neutron emission profile measurement is started with I_p rump up timing signal of ZENKEI system. Users can refer the wave form data of each channel using the soft, for example DAISY [25], together with other data, after several minutes from the end of discharge.

3.4 First Result of neutron emission profile measurement

The Stilbene neutron detectors have been located at the detector box of neutron emission profile monitor illustrated in Fig.3.3 and applied to JT-60U DD experiments.

3.4.1 Linearity of count rate

The count rate limit of the Stilbene neutron detector is restricted by the gate
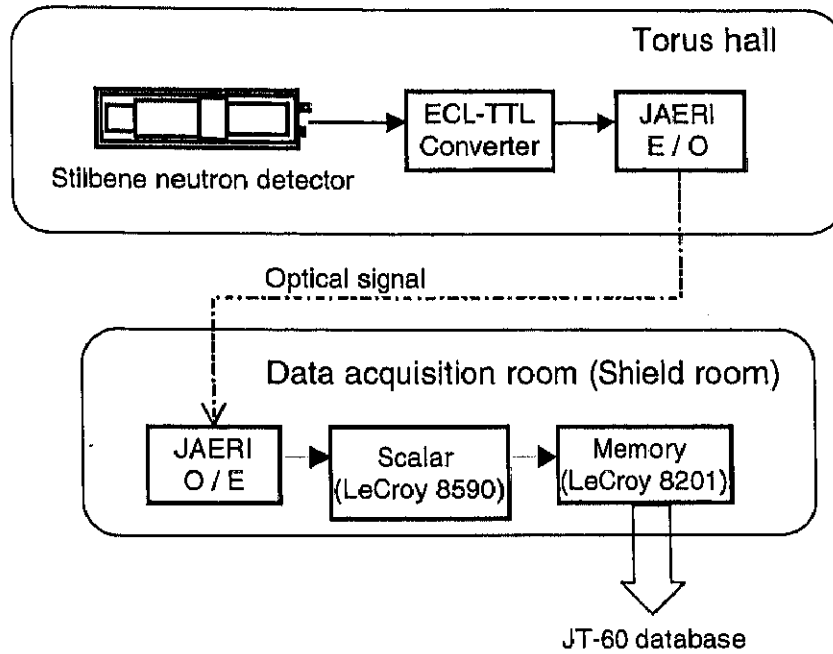
Figure 3.18 *Basic data flow diagram of neutron emission profile measurement*

integration time of the discrimination circuit and depends on the sum of neutron flux and gamma-ray flux because the Stilbene scintillator itself is sensitive to gamma-rays.

Firstly, we confirmed the linearity of the count rate of the Stilbene neutron detector prior to the measurement of neutron emission profile in the JT-60U experiment. The relation between the count rate of Stilbene neutron detector whose sight line passes through the plasma axis and total neutron emission rate measured by a ^{235}U fission chamber is shown in Fig.3.19. We can see that the count rate of Stilbene neutron detector is proportional to the neutron flux measured by ^{235}U fission chamber below the total neutron emission rate of about 3×10^{15} n/s. This comparison indicates that the maximum count rate of Stilbene neutron detector is about $1\text{-}1.3 \times 10^{5}$ counts/s. The maximum count rate of the Stilbene neutron detector is smaller than NE213 ($\sim 10^{6}$ cps).
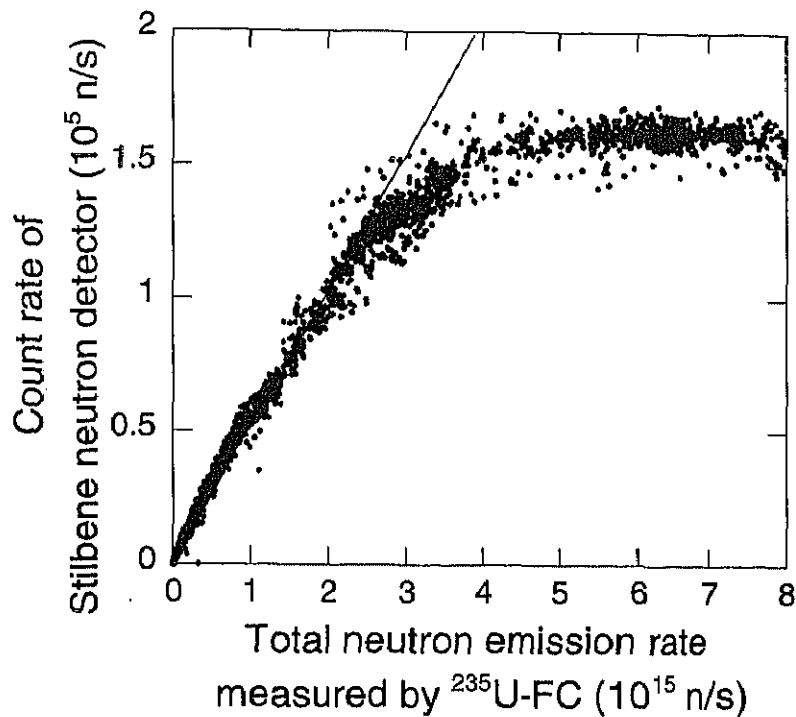
Figure 3.19 *Linearity of the Stilbene neutron detector for total neutron emission rate by U-FC*

3.4.2 Collimator effect

In Sec.3.3.3 the effect of neutron shielding and attenuation for neutron emission profile monitor by using MCNP. However, it is important to confirm that the collimator array actually shield against neutron out of the sight line of each channel. Therefore by using neutron plug which is filled with Polyethylene beads, the shielding test of neutron collimator was performed. We close one of collimator channel by the neutron plug, then compared the neutron signal of this channel between closed state (CLOSE) and usual open state (OPEN) in the similar experimental scenario.

Figure 3.20 shows the time trace of measured emission rate of each channel. Figure 3.20 (a) is OPEN, (b) is CLOSE. The thick line of each figure means the channel of closed collimator tube. Comparing Fig. 3.20 (a) with (b), we can see that the neutron signal of the CLOSE channel reduces to less than 10 % as much as OPEN. We performed this test for innermost channel (ch.1) and outermost channel (ch.6). The ratio of neutron counts of CLOSE to OPEN for innermost and outermost channel is about 0.09 and 0.04,
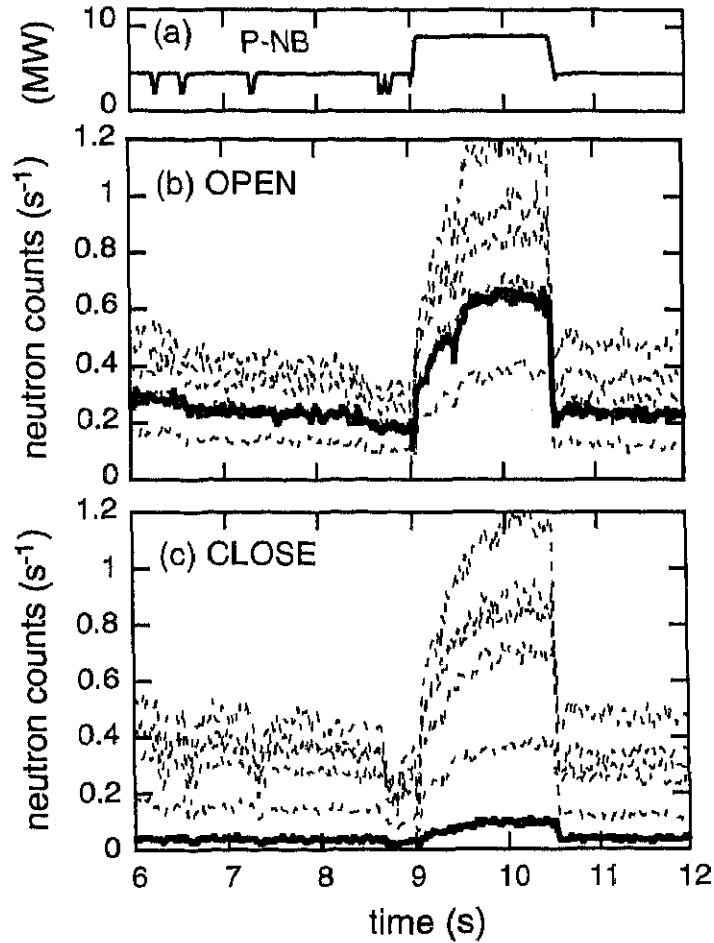
Figure 3.20 *(a) Time trace of beam injection power, (b) neutron signal of each channel for normal case (OPEN), (c) channel 6 is closed by filling with Polyethylene beads (CLOSE). Thick lines of (b) and (c) show the difference by closing the collimator.*

respectively. Also we can see that there is no influence for signals of the other channels.

Therefore, taking into account that neutron plug is the state of Polyethylene beads, it is confirmed that neutron emission profile monitor is surely working in the JT-60U experiment.

3.4.3 First measurement of neutron emission profile

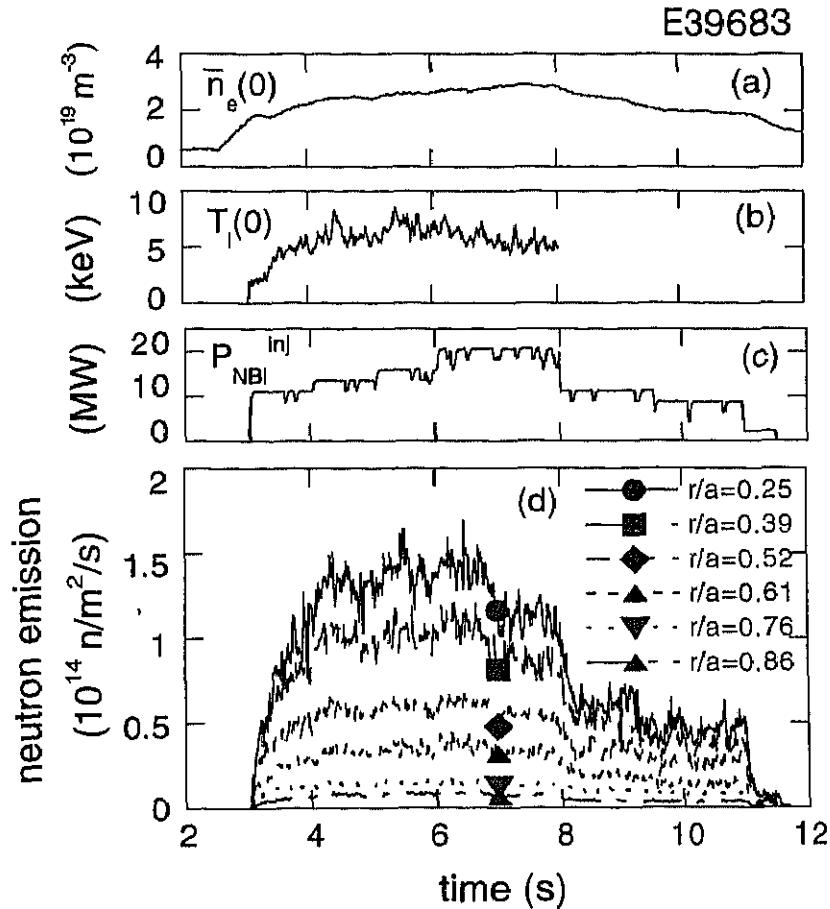The system of neutron emission profile measurement was applied to deuterium

Figure 3.21 *Wave forms of ELMy-H mode plasma. (a) Central line-averaged electron density, (b)Central ion temperature, (c) Total beam injection power, and (d) Neutron signals for each channel*

experiments of JT-60U. In Fig.3.21 waveforms of a typical ELMy H-mode plasma are shown. Here, I_p is 1 MA and B_T is 2.0 T. Significant instabilities are not observed in the core plasma region throughout this discharge. The ion temperature measurement was not available after 8s. The plasma configuration at t = 7.4 s is shown in Fig.3.22. The sight line of the innermost channel passes through $\rho \sim 0.25$ and outermost channel passes through $\rho \sim 0.86$, where ρ is the normalized minor radius. Neutron signals during neutral beam injection are shown in Fig.3.21 (d). The data of Fig.3.21 (d) are derived with geometry factor taken into account. The signal of the innermost channel is the largest.
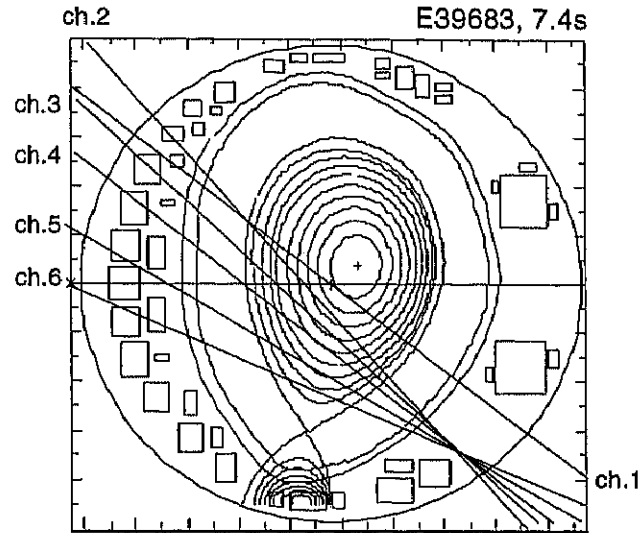
Figure 3.22 *The plasma configuration at t = 7.4 s, E39683 and the line-of-sight are illustrated. The innermost channel (ch.1) passes through r/a~0.25. and from ch.2 to ch.6 pass through r/a ~ 0.39, 0.52, 0.61, 0.76, and 0.86, respectively*

Figure3.24 shows a line-integrated neutron emission profile (circle) compared with calculation (square) from TOkamak Prediction and Interpretation Code System (TOPICS) [26] in JT-60U at t =7.4s. TOPICS is tokamak transport code system for the systematic transport studies in experimental data analysis and theory-based performance analysis, both in steady state and in time evolution. In the calculation by TOPICS the measured profile of ion temperatures $(T_i(\rho))$, electron temperature $(T_e(\rho))$, electron density $(n_e(\rho))$ and effective ion charge $(Z_{eff}(\rho))$ are used. Also the information on neutral beam injection, for example used ion source, its acceleration voltage and beam power, are necessary. $T_i(\rho)$ are measured by charge exchange recombination spectroscopy. $Z_{eff}(\rho)$ is assumed to be constant in the plasma and evaluated using a profile of Bremsstrahung, $n_e(\rho)$ and $T_e(\rho)$ by Thomson scattering. $n_e(\rho)$ and $T_e(\rho)$, $T_i(\rho)$ at t = 7.4 s are shown in Fig.3.23 (a) and (b), respectively. Carbon was the dominant impurity in this discharge, and the Z_{eff} is evaluated 2.9 at 7.4 s. In the TOPICS
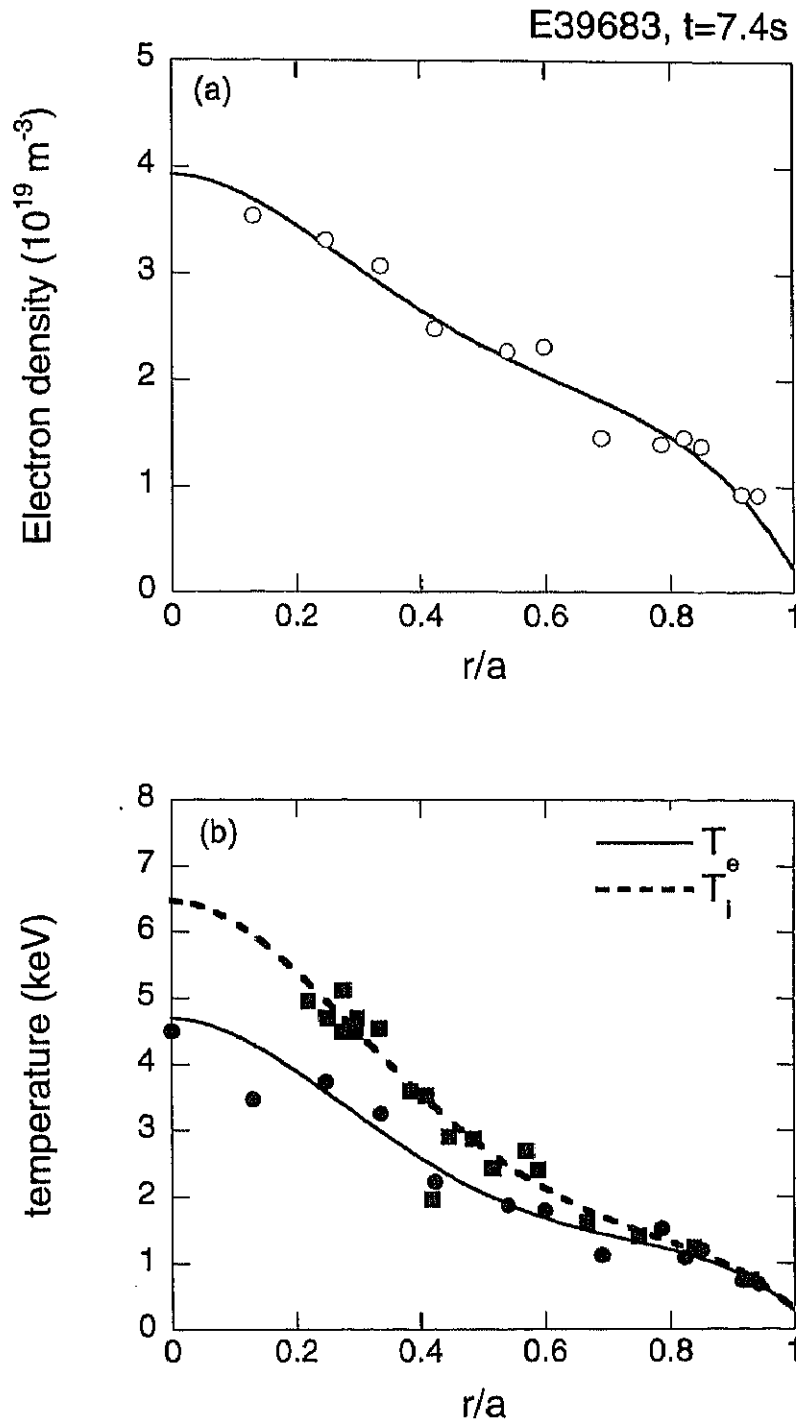
61

Figure 3.23 *profile of (a) Electron density and (b) electron (solid line), ion (broken line) temperature at t = 7.4s, E39683.*
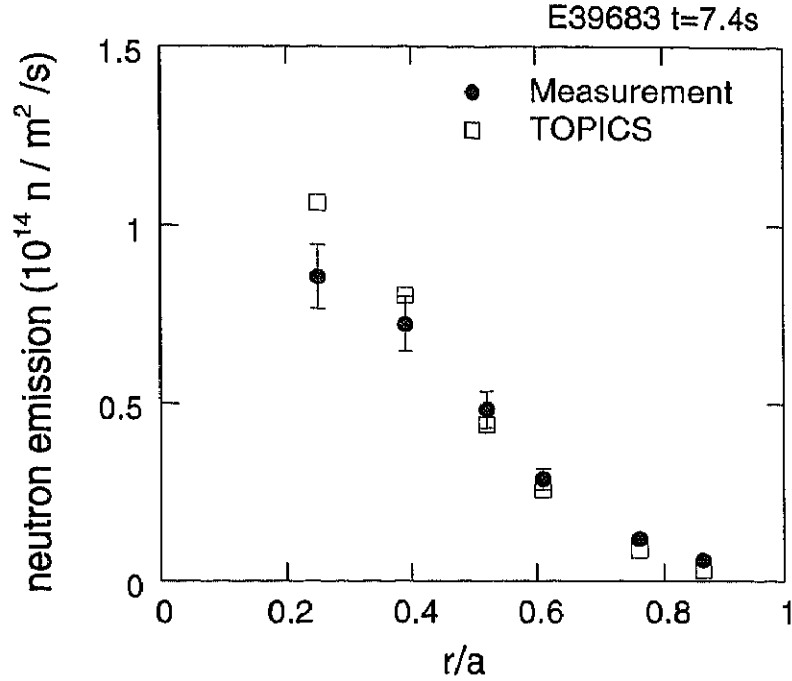
Figure 3.24 *Profile of line-integrated neutron emission. Circles show the measured result by the Stilbene neutron detector, square shows the calculated result by the TOPICS*

code the ionization source of injected neutral beam is calculated and then density profile of beam component n_b is calculated using Stix's stationary solution [27] as a velocity distribution function. Ion density n_i is given by $n_i = n_{th} + n_b$, where n_{th} is the thermal component, Then the DD neutron profile emitted by thermal-thermal (TH), beam-thermal (BT) and beam-beam (BB) reaction is calculated. In this calculation the fraction of TH, BT, BB neutron is 11%, 69%, 20%, respectively. In Fig.3.24 the line-integrated total neutron (TH+BT+BB) signal along each sight line calculated by TOPICS is shown. Though there is 30% error in innermost channel between measurement and calculation, there is an agreement within 10% error in the other channels.

3.5 Summary

As mentioned above, in order to measure the neutron emission profile by discriminating gamma-rays, we introduced the Stilbene neutron detector, which

combines a Stilbene organic crystal scintillator with a neutron-gamma pulse shape discrimination circuit, and performed the several tests. The effect of neutron scattering and attenuation in the collimator walls is estimated by using MCNP. Then, we installed the Stilbene neutron detectors at the detector box of neutron emission profile monitor illustrated in Fig.3.3 and applied them to JT-60U DD experiments.

For the several tests of the Stilbene neutron detector, we have verified that the CONTROL output of the Stilbene neutron detector suppresses gamma-ray sufficiently and provides the signal only when neutron is detected, its applicability to deuterium discharge of JT-60U are demonstrated.

In neutral beam heated plasma of the JT-60U experiments, the neutron profile measured by Stilbene neutron detector is in a reasonable agreement with the calculation result by the TOPICS code

References

[1] L. C. Johonson, Cris W. Barnes, Rev. Sci. Instru. **70** (1999) 1145

[2] F. B. Marcus, et al., in Diagnostics for Experimental Thermonuclear Fusion Reactor 2 1997 (Proc. Int. Workshop on Diagnostics for ITER, Varenna, 1997) Plenum Press, New Youk (1998) 419

[3] F. B. Marcus, et al., Rev. Sci. Instrum. **68** (1997) 514

[4] J. M. Aams *et al.*, Nucl. Instr.and Meth. **A329** (1993) 277

[5] A. L. Roquemore *et al.*, Rev. Sci. Instrum. **61** (1990) 3163

[6] F. D. Brooks, Nucl Instr. and Meth. **162** (1979) 477

[7] J. M. Adams, G. White, Nucl. Instr. and Meth. **156** (1978) 459

[8] F. D. Brooks, Nucl Instr. and Meth. **4** (1959) 151

[9] G. Gamov, Z. Phys. **51** (1928) 204.

[10] D. D. Clayton, Principles of Stellar Evolution and Nucleosynthesis, McGraw-Hill, New York, 1968.

[11] B.H. Duane, Fusion cross section theory in Annual Report on CTR Technology, Report BNWL-1685, Batelle Pacic Northwest Lab, Richland, 1972.

[12] D.L. Book, NRL Plasma Formulary (revised) NRL 0084-4040, Naval Research Laboratory, Washington DC 20375, 1987.

[13] A. Peres, J. Appl. Phys. **50** (1979) 5569.

[14] H.-S. Bosch, G.M. Hale, Nucl. Fusion **32** (1992) 611.

[15] A.M. Lane, R. G. Thomas, Rev. Mod. Phys. **30** (1958) 57.

[16] J. G. Cordey, K .D. Marx, M. G. McCoy, A. A. Mirin, M. E. Resnik, J. Comput. Phys. **28** (1978) 115.

[17] D. R. Mikkelsen, Nucl. Fusion **29** (1989) 1113.

[18] G. H. Miley, H. Zowner, N. Ivich, Fusion cross sections and reactivities Report COO-2218-17, University of Illinois, Urbana, 1974.

[19] D. Slaughter, J. Appl. Phys. **54** (1983) 1209.

[20] J. L. Tuck, Nucl. Fusion **1** (1961) 201.

[21] E. A. Lorch, Int. J. Appl. Radiat. Isptopes **24** (1973) 585

[22] R. Craun, D.L. Smith, Nucl. Instr.and Meth. **80** (1974) 239

[23] T. Nakamura *et al.*, Proc. Int. Ion Eng.ongress-ISIAT **83** (1983) 567

[24] J. F. Briesmeister, (Ed.), LA-12625-M, Los Alamos National Laboratory (1997)

[25] Y. Oginoya, et al., JAERI-M 94-040 (1994)

[26] T. Nishitani *et al.*, Nucl. Fusion **34** (1994) 1069

[27] T. H. Stix, Plasma Phys. **14** (1972) 367